Chinese Chemical Letters 36 (2025) 109774

Contents lists available at ScienceDirect

Chinese Chemical Letters

journal homepage: www.elsevier.com/locate/cclet

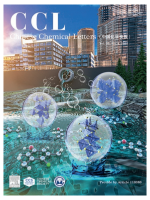

# Room-temperature synthesis of $Co(OH)_2/Mo_2TiC_2T_x$ hetero-nanosheets with interfacial coupling for enhanced oxygen evolution reaction

Lu Dai[a,b], Yuxin Ren[a,b], Shuang Li[a,b,*], Meidi Wang[a,b], Chentao Hu[a,b], Ya-Pan Wu[a,b], Guangtong Hai[c], Dong-Sheng Li[a,b,*]

[a] *College of Materials and Chemical Engineering, Key Laboratory of Inorganic Nonmetallic Crystalline and Energy Conversion Materials, China Three Gorges University, Yichang 443002, China*
[b] *Hubei Three Gorges Laboratory, Yichang 443007, China*
[c] *Beijing Advanced Innovation Center for Materials Genome Engineering, Beijing Key Laboratory of Function Materials for Molecule & Structure Construction, School of Materials Science and Engineering, University of Science and Technology Beijing, Beijing 100083, China*

ARTICLE INFO

*Article history:*
Received 16 January 2024
Revised 26 February 2024
Accepted 14 March 2024
Available online 16 March 2024

*Keywords:*
ZIF
$Co(OH)_2$
MXenes
Interfacial coupling
OER

ABSTRACT

Constructing high-performance electrocatalysts for oxygen evolution reaction (OER) using a simple and economical strategy is considerably meaningful yet still challenging. Herein, $Co(OH)_2/Mo_2TiC_2T_x$ (where $T_x$ represents the surface functional groups, -O, -OH and -F) hetero-nanosheets were facilely prepared by the *in situ* topochemical transformation at room temperature towards efficient OER. The integrity of $Co(OH)_2$ nanosheets and $Mo_2TiC_2T_x$ nanosheets affords interfacial coupling to optimize the electronic structures of Co and Mo ions, which endows the high electron transfer efficiency and rapid reaction kinetics. As a result, the $Co(OH)_2/Mo_2TiC_2T_x$ hetero-nanosheets exhibit excellent OER performances with low overpotentials of 283 mV on glass-carbon electrode, and 227 mV on nickel foam at 10 mA/cm$^2$. Furthermore, the decent anti-alkali ability underpins superior operational stability exceeding 100 h, demonstrating grand potential in practical applications. This work provides a new insight for the synthesis of efficient and cost-effective two-dimensional (2D) material-based electrocatalysts.

Hydrogen energy presents a promising solution to alleviate the energy crisis and environmental pollution owing to its zero-carbon emission and high calorific value [1,2]. Electrochemical water splitting, consisting of hydrogen evolution reaction (HER) at the cathode and oxygen evolution reaction (OER) at the anode, is an eco-friendly and efficient technology for hydrogen production [3]. OER is a four-electron transfer process that suffers from a higher energy barrier and sluggish kinetics, so it is regarded as the bottleneck step of the whole water splitting [4,5]. Therefore, finding an efficient and stable OER catalyst to reduce the anode reaction overpotential is vital to improve the efficiency of hydrogen production. So far, precious metal-based catalysts (such as $RuO_2$, and $IrO_2$) show optimum OER activity, however, their large-scale practical applications are still hindered by high cost and low storage capacity [6,7]. Consequently, the development of highly efficient non-precious metal catalysts is crucial for the future applications of OER.

To date, a great deal of non-precious metal catalysts has been reported to boost OER performance. Thereinto, transition metal hydroxides (TMHs) have attracted increasing attention because of their large specific surface area, abundant metal active sites and low cost [8–11]. Nevertheless, inferior electrical conductivity and strong aggregation tendency of TMHs lead to low catalytic activity and unideal stability in OER process [12–14]. Metal-organic frameworks (MOFs) have become promising materials in various applications due to their unique structural advantages [15,16]. In recent years, some studies have shown that TMHs derived from MOFs precursors by means of hydrolysis, chemical etching, ion-exchange, *etc.* can effectively restrain their agglomeration [17–21]. For instance, Chen *et al.* used 2D Hofmann-MOFs as self-sacrificial templates to synthesize FeNi-LDH nanosheets *via* a hydrolysis transformation assisted by $NaBH_4$, which effectually inhibited the self-stacking of LDHs, resulting in excellent OER activity [19]. Che group reported the self-transforming $Co(OH)_2$ nanosheet arrays from ZIF-67, which bring high exposure of active sites for OER [20]. Although the unique structure of TMHs obtained from the MOFs template endows improved OER performance, it is still necessary to take other measures to further boost their OER conductivity and reactivity.

---

* Corresponding authors.
*E-mail addresses:* lidongsheng1@126.com (S. Li), lishmail@126.com (D.-S. Li).

https://doi.org/10.1016/j.cclet.2024.109774

Recently reported that integrating TMHs with other functional materials (such as MXene, graphene, and $NiP_x$) to construct heterostructured composites is a promising way to solve the aforementioned problems [22–24]. This is mainly attributed to the fact that interfacial coupling can induce the redistribution of local electrons and regulate the electronic structure of atoms, thereby improving electrochemical reactivity, conductivity and stability [25,26]. Among the functional materials, MXenes are deemed as ideal substrate material to fabricate heterostructures for effectively modulating the electronic structures of target catalysts. Since the abundant surface negative terminations produced during the synthesis process, MXenes can easily anchor the functional units to form versatile hybrids *via* electrostatic absorption, hydrogen bonding, or covalent bonding [27–29], which is important for inhibiting MXene self-restacking and generating strong interface interactions at the molecular level. They are usually written as $M_{n+1}X_nT_x$, where M is an early transition metal, X is C and/or N, $T_x$ represents surface functional groups such as -O, -OH and -F [30]. As the most studied material, $Ti_3C_2T_x$ has been widely used as a substrate material to design extended heterostructures for energy storage and conversion applications [31,32]. In 2015, Anasori *et al.* discovered an ordered double-transition bimetallic $Mo_2TiC_2T_x$ MXene with two layers of Mo atoms located on the outer side, while Ti atoms occupy the middle metal layer [33,34]. Unlike the conventional $Ti_3C_2T_x$, Mo atoms are present on the surface of $Mo_2TiC_2T_x$, thus the type of interface bonds can be tuned when it is combined with other components [35–38]. Moreover, related research has shown that $Mo_2TiC_2T_x$ possesses a relatively stronger Ti-C chemical bond than that of $Ti_3C_2T_x$ [39]; however, compared with $Ti_3C_2T_x$, there is relatively less research on coupling $Mo_2TiC_2T_x$ with other functional materials to regulate the OER performance [40].

Herein, $Co(OH)_2/Mo_2TiC_2T_x$ hetero-nanosheets were prepared using ZIF-67 as a raw material through simple topochemical transformations at room temperature. Detailed XPS and XANES analyses reveal that the interfacial coupling between $Co(OH)_2$ and $Mo_2TiC_2T_x$ enables the electron transfer from $Co(OH)_2$ to $Mo_2TiC_2T_x$, thereby increasing the valence state of Co ions and the electron density around the Mo species, which contributes to the high OER reactivity. Moreover, in the process of topological structure conversion, ZIF-67 was *in situ* converted into $Co(OH)_2$ nanosheets, which strongly combined with the $Mo_2TiC_2T_x$ nanosheets. Such hetero-nanosheets endow the composites with abundant active sites and well-developed electron transport channels as well as robust structural stability. As a result, the $Co(OH)_2/Mo_2TiC_2T_x$ hetero-nanosheets exhibit excellent OER performances with low overpotentials of 283 mV on glass-carbon electrode, 227 mV on nickel foam at 10 mA/cm$^2$ and can be stable for 100 h in alkaline solution, holding great promise for practical applications.

As depicted in Fig. S1 (Supporting information), $Co(OH)_2/Mo_2TiC_2T_x$ hetero-nanosheets were synthesized through a convenient room temperature topochemical transformation strategy, involving the successive preparation of $Mo_2TiC_2T_x$ and ZIF-67/$Mo_2TiC_2T_x$ composites. The details of the procedure are as follows: $Mo_2TiC_2T_x$ nanosheets were first obtained by a combined method of NaF/HCl etching and liquid exfoliation. Notably, during the etching procedure, Al atoms were removed from between layers, while fluorine and oxygen-containing functional groups were adsorbed on the surface of Mo atoms. These terminated $Mo_2TiC_2T_x$ nanosheets can easily adsorb the $Co^{2+}$ ions in cobalt salts by the electrostatic interactions, which greatly facilitates the direct growth of ZIF-67 on $Mo_2TiC_2T_x$ nanosheets. Subsequently, under the continued ultrasound process, the ZIF-67 in ZIF-67/$Mo_2TiC_2T_x$ composites undergoes rapid hydrolysis and self-transforms into $Co(OH)_2$ nanosheets, thereby leading to the *in-situ* formation of tightly contacted $Co(OH)_2/Mo_2TiC_2T_x$ hetero-nanosheets. The $Co(OH)_2/Mo_2TiC_2T_x$ (*i.e.*, $Co(OH)_2/Mo_2TiC_2T_x$-3 in the performance section) with the 40 mg $Mo_2TiC_2T_x$ loading is discussed in the following characterizations because it shows the highest electrocatalytic activity, see below. And the inductively coupled plasma emission spectrometer (ICP-OES) reveals the content of Co, Mo and Ti in this composite is 42.22 wt%, 8.5 wt% and 2.17 wt%, respectively, so the hybrid atomic ratio of Co:Mo:Ti is approximately 8:1:0.5.

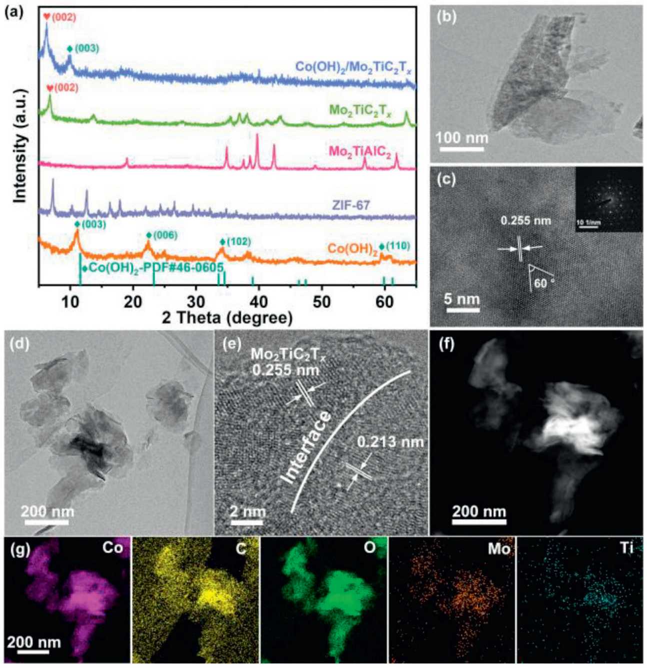

**Fig. 1.** (a) XRD patterns of the as-obtained samples. (b) TEM image of $Mo_2TiC_2T_x$ nanosheets. (c) HRTEM image and the corresponding FFT (inset) of $Mo_2TiC_2T_x$ nanosheet. (d) TEM image of $Co(OH)_2/Mo_2TiC_2T_x$ nanosheets. (e) HRTEM image of $Co(OH)_2/Mo_2TiC_2T_x$ nanosheet. (f, g) HAADF and corresponding EDS element mapping images of $Co(OH)_2/Mo_2TiC_2T_x$ nanosheets.

X-ray diffraction (XRD) technique was performed to study the structural information of the as-prepared samples, as shown in Fig. 1a. Compared with $Mo_2TiAlC_2$ precursor, the characteristic peak at 39° disappears of $Mo_2TiC_2T_x$ and the (002) peak appears at 6.9°, indicating the successful transformation from the $Mo_2TiAlC_2$ phase to the $Mo_2TiC_2T_x$ structure *via* NaF/HCl etching. Meanwhile, the XRD pattern of the obtained ZIF-67 precursor is in good match with the previous report [20]. Under continuous ultrasound treatment at room temperature, ZIF-67 experiences a topochemical transformation and its diffraction peaks completely disappear. Moreover, a set of diffraction peaks corresponding to $\alpha$-$Co(OH)_2$ appear (JCPDS card No. 46–0605), which confirms that ZIF-67 is completely converted to $Co(OH)_2$ at room temperature. When $Mo_2TiC_2T_x$ is added into the above system, the XRD pattern of the product shows the characteristic diffraction peaks of $Co(OH)_2$ and $Mo_2TiC_2T_x$, demonstrating the successful preparation of $Co(OH)_2/Mo_2TiC_2T_x$ composite. Additionally, compared with pure $Mo_2TiC_2T_x$, the (002) peak of $Co(OH)_2/Mo_2TiC_2T_x$ shifts towards a lower angle direction (from 6.9° to 6.3°), indicating that coupling $Co(OH)_2$ can increase the layer spacing of $Mo_2TiC_2T_x$ nanosheets, thereby preventing them from stacking. The microstructure information of these samples was detected by scanning electron microscopy (SEM) and transmission electron microscopy (TEM). As displayed in Fig. S2a (Supporting information), the etched $Mo_2TiC_2T_x$ displays a typical accordion-like structure. After ultrasonic treatment in NMP, the layered $Mo_2TiC_2T_x$ was exfoliated into ultrathin nanosheets with a lateral size of

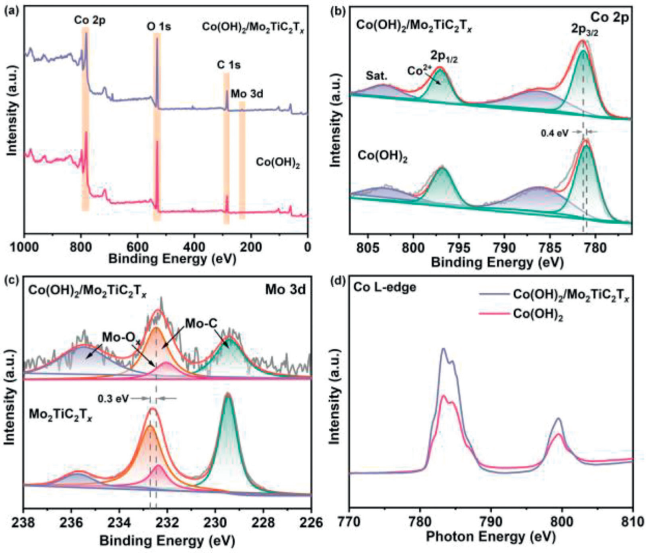

**Fig. 2.** XPS spectra of (a) survey, (b) Co 2p, (c) Mo 3d and (d) Co L-edge.

about several hundreds of nanometers, as is confirmed by the TEM image (Fig. 1b). In the HRTEM image (Fig. 1c), the lattice fringe of 0.255 nm corresponds to the diffraction peak at $2\theta = 35°$ of Mo$_2$TiC$_2$T$_x$. Furthermore, from the inserted fast Fourier transform (FFT) image, the typical hexagonal symmetry of Mo$_2$TiC$_2$T$_x$ nanosheets can be seen. The SEM image in Fig. S2c (Supporting information) shows that Co(OH)$_2$ derived from rhombohedral dodecahedron ZIF-67 (Fig. S2b in Supporting information) also possesses nanosheets structure, which ensures intimate contact with Mo$_2$TiC$_2$T$_x$ nanosheets, providing abundant active sites and facilitating electron transport channels. The SEM (Fig. S2d in Supporting information) and TEM (Fig. 1d) images confirm that the hetero-nanosheets morphology of as-obtained Co(OH)$_2$/Mo$_2$TiC$_2$T$_x$ with a lateral size of several hundred nanometers, and the high transparency of TEM indicates their ultrathin feature. Moreover, the corresponding HRTEM image of the Co(OH)$_2$/Mo$_2$TiC$_2$T$_x$ (Fig. 1e) demonstrates the formation of a heterogeneous interface between Co(OH)$_2$ and Mo$_2$TiC$_2$T$_x$. Wherein, the lattice fringe of 0.213 nm belongs to the (200) crystal plane of CoO, since the ultrathin Co(OH)$_2$ nanosheets are extremely sensitive to electron beam irradiation and can be quickly converted to CoO under electron beam [41], which is further confirmed by TEM and HRTEM images of the single Co(OH)$_2$ nanosheets (Figs. S3a-c in Supporting information). Meanwhile, the lattice fringe of 0.255 nm matches well with the diffraction peak at 35° of Mo$_2$TiC$_2$T$_x$. These two crystal planes are consistent with that of individual Co(OH)$_2$ and Mo$_2$TiC$_2$T$_x$, respectively, further proving the existence of heterogeneous interfaces in Co(OH)$_2$/Mo$_2$TiC$_2$T$_x$ hetero-nanosheets. The heterostructure is believed to play an important role in boosting electron transfer and stability as well as tuning electron structure [42]. In addition, the high-angle annular dark-field (HAADF) image of Co(OH)$_2$/Mo$_2$TiC$_2$T$_x$ and the corresponding element mapping images show a uniform distribution of Co, C, O, Mo and Ti (Figs. 1f and g) across the nanosheet. These results confirm the achievement of Co(OH)$_2$/Mo$_2$TiC$_2$T$_x$ hetero-nanosheets.

X-ray photoelectron spectroscopy (XPS) was used to study the chemical valence state of Co(OH)$_2$/Mo$_2$TiC$_2$T$_x$ and the electronic interaction between Co(OH)$_2$ and Mo$_2$TiC$_2$T$_x$. As shown in Fig. 2a, the survey XPS spectra further confirm the elemental composition of the samples. The high-resolution Co 2p spectrum of the Co(OH)$_2$ demonstrates the Co 2p$_{3/2}$ (781.0 eV) and Co 2p$_{1/2}$ (796.8 eV) peaks as well as two shakeup satellite peaks, respectively, indicating the valence state of Co species is +2 (Fig. 2b). Interestingly, compared with the Co(OH)$_2$, the Co 2p peaks of Co(OH)$_2$/Mo$_2$TiC$_2$T$_x$ are shifted towards higher binding energies, implying that a decrease in local charge density of Co ions accompanied with higher valence state [32]. The Mo 3d spectrum of Mo$_2$TiC$_2$T$_x$ (Fig. 2c) can be divided into four peaks, of which the peak located at 229.5 and 232.7 eV correspond to the Mo 3d$_{5/2}$ and 3d$_{3/2}$ levels for the Mo-C bonds, which shows that 4+ is the dominant oxidation state. Two small peaks at 232.4 and 235.7 eV belong to Mo 3d$_{5/2}$ and 3d$_{3/2}$ levels of surface Mo-O bonds (Mo$^{6+}$), which can be attributed to the surface oxide-containing terminations [36,40]. Compared with Mo$_2$TiC$_2$T$_x$, an obvious shift of Mo-C bond to the lower binding energy is observed for the Co(OH)$_2$/Mo$_2$TiC$_2$T$_x$, showing an increase in the charge density around the Mo atoms. Moreover, in the XPS O 1s spectra (Fig. S4 in Supporting information), except for the Co-OH peak (531.5 eV) and adsorbed water peak (532.9 eV), a new peak at 530.5 eV attributed to the Co-O-Mo bonds appears in the Co(OH)$_2$/Mo$_2$TiC$_2$T$_x$, which are favourable for the electron transfer between Co(OH)$_2$ and Mo$_2$TiC$_2$T$_x$ [43,44]. To go further, the interface electronic interaction between Co(OH)$_2$ and Mo$_2$TiC$_2$T$_x$ in Co(OH)$_2$/Mo$_2$TiC$_2$T$_x$ hetero-nanosheets was also examined by soft X-ray adsorption near-edge structure (XANES). As shown in Fig. 2d, the Co L-edge splits into lower energy L$_3$-edge and higher energy L$_2$-edge due to spin-orbit splitting. Although the peak positions of Co L-edge for Co(OH)$_2$/Mo$_2$TiC$_2$T$_x$ hetero-nanosheets have almost no change by comparison with that of Co(OH)$_2$, their peak area is higher than that of Co(OH)$_2$. As is known, the normalized peak area of the sample can explain the occupied state of electrons. The larger peak area shows that there are more empty orbits with higher valence state [45]. Compared with Co(OH)$_2$, the Co ions in Co(OH)$_2$/Mo$_2$TiC$_2$T$_x$ have more empty orbitals, indicating that higher Co ions are generated, which is consistent with the results of Co 2p XPS. High valence Co ions have been proven to be beneficial for improving OER reactivity [46,47].

To shed light on the role of interfacial coupling play in the OER, the electrocatalytic performances of the obtained Co(OH)$_2$/Mo$_2$TiC$_2$T$_x$ hetero-nanosheets, pure Co(OH)$_2$ and Mo$_2$TiC$_2$T$_x$ were examined using a three-electrode system in 1.0 mol/L KOH solution at room temperature. Moreover, to achieve optimal OER performance, Co(OH)$_2$/Mo$_2$TiC$_2$T$_x$ composites with different amounts of Mo$_2$TiC$_2$T$_x$ were synthesized and tested. As shown in Fig. 3, the OER performance of the sample with 0.285 mg/cm$^2$ loaded on the glass-carbon (GC) electrode was first evaluated. Fig. 3a shows the polarization curves of different samples, in which Co(OH)$_2$/Mo$_2$TiC$_2$T$_x$-3 has the best OER activity. The overpotentials that correspond to Co(OH)$_2$ and four Co(OH)$_2$/Mo$_2$TiC$_2$T$_x$ composites at 10 mA/cm$^2$ are 323, 309, 298, 283 and 358 mV, respectively (Fig. 3b). From the above values, it can be seen that the amount of Mo$_2$TiC$_2$T$_x$ has a significant impact on the OER activity of the composites, which may be attributed to the strength of interface coupling. The Co(OH)$_2$/Mo$_2$TiC$_2$T$_x$-3 achieves an optimized interface coupling effect. Moreover, to reveal the effect of the surface Mo atom on the OER activity of Mo$_2$TiC$_2$T$_x$, Co(OH)$_2$/Ti$_3$C$_2$T$_x$ composites were also prepared (Fig. S5 in Supporting information) and tested. Compared with the Co(OH)$_2$/Mo$_2$TiC$_2$T$_x$-3, the Co(OH)$_2$/Ti$_3$C$_2$T$_x$ has a larger $\eta_{10}$ of 334 mV, which directly proves the beneficial role of surface Mo atoms on Mo$_2$TiC$_2$T$_x$ OER process. The corresponding Tafel slope in Fig. 3c further unravel the best OER kinetics of the Co(OH)$_2$/Mo$_2$TiC$_2$T$_x$-3 (80 mV/dec) by comparison with the Co(OH)$_2$/Mo$_2$TiC$_2$T$_x$-1 (116 mV/dec), Co(OH)$_2$/Mo$_2$TiC$_2$T$_x$-2 (95 mV/dec), Co(OH)$_2$/Mo$_2$TiC$_2$T$_x$-4 (108 mV/dec) and Co(OH)$_2$/Ti$_3$C$_2$T$_x$ (93 mV/dec), which could be attributed to the moderate interfacial coupling between Mo$_2$TiC$_2$T$_x$ and Co(OH)$_2$.

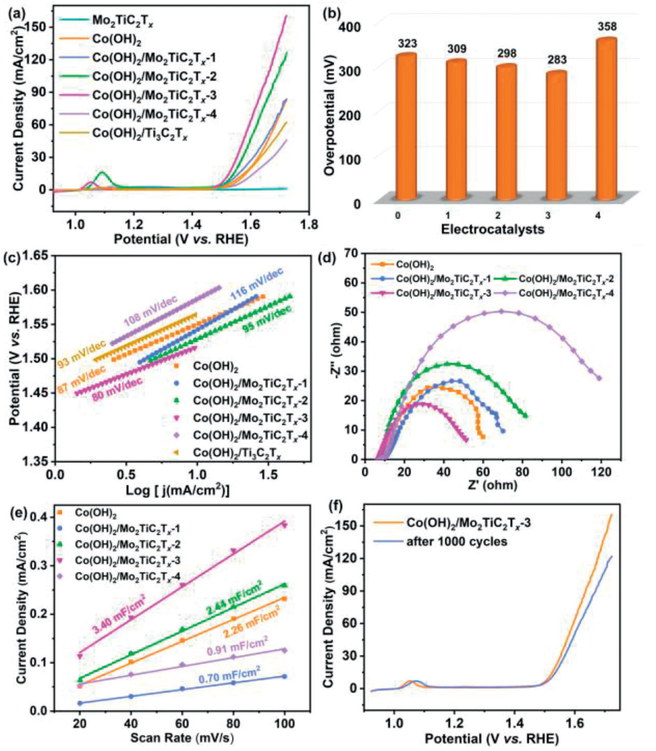

**Fig. 3.** OER performances of catalysts coated on GC electrode: (a) Polarization curves. (b) Comparison of the overpotential of different samples at 10 mA/cm$^2$. (c) The corresponding Tafel plots. (d) Nyquist plots. (e) Liner fitting of $C_{dl}$ of the catalysts versus scan rate for the estimation of the ECSA. (f) LSV curves of $Co(OH)_2/Mo_2TiC_2T_x$ initially and after 1000 CV cycles.

The charge transfer kinetics of as-prepared catalysts during the OER process were further estimated by electrochemical impedance spectroscopy (EIS). As shown in Fig. 3d, compared with other samples, the $Co(OH)_2/Mo_2TiC_2T_x$-3 has the smallest semicircular diameter with charge-transfer resistance of 44 Ω, suggesting its fastest charge transfer kinetics, which is consistent with the result of the Tafel slope. The double-layer capacitance ($C_{dl}$) was measured in the non-Faraday range (Fig. S6 in Supporting information) to assess the electrochemical surface area (ECSA) of the samples. As displayed in Fig. 3e, among all the catalysts, $Co(OH)_2/Mo_2TiC_2T_x$-3 has the highest $C_{dl}$ value of 3.40 mF/cm$^2$, indicating that more active sites are exposed for OER, which contributes to the excellent OER activity. Besides, stability is an important indicator for the practical application of catalysts. Therefore, a long-term CV cycling test was carried out to assess the stability of the $Co(OH)_2/Mo_2TiC_2T_x$-3. As shown in Fig. 3f, slight differences between LSV curves can be observed before and after 1000 CV cycles, demonstrating the good durability of the $Co(OH)_2/Mo_2TiC_2T_x$-3 hybrid nanosheets.

To explore whether the performance of the $Co(OH)_2/Mo_2TiC_2T_x$ remains unchanged when the amount of catalyst is increased by dozens of times. The obtained samples were coated on the common nickel foam (NF) collector with a high loading amount of 10 mg/cm$^2$ to further investigate the OER activity, which is conducive to the industrial application. As shown in Figs. 4a and b, Figs. S7 and S8 (Supporting information), the comparative trend for OER performance of these samples coated on NF is similar to that of the samples with GC electrode as the substrate, where $Co(OH)_2/Mo_2TiC_2T_x$-3 still has the best OER activity of 227 mV at 10 mA/cm$^2$, demonstrating the outstanding substrate-independent OER activity. This overpotential is also comparable to previously reported advanced OER electrocatalysts, as displayed in Table S1 (Supporting information). Moreover, the chronopotentiometry curve at 10 mA/cm$^2$ (Fig. 4c) shows no significant change in OER activity over 100 h, indicating that the $Co(OH)_2/Mo_2TiC_2T_x$-3 has excellent long-term OER stability. Besides, the XRD and TEM were conducted to confirm the structure and morphology of $Co(OH)_2/Mo_2TiC_2T_x$-3 after a long-term chronopotentiometry test (Fig. S9 in Supporting information). By the analysis of post-OER characterization, $Co(OH)_2/Mo_2TiC_2T_x$ still presents the nanosheet morphology, while partially $Co(OH)_2$ is oxidized to CoOOH during OER process. To reveal the OER intrinsic activity of the obtained catalysts, density functional theory (DFT) was performed to study the free energy of OER intermediates. In the calculation, the structural models of the reconstructed CoOOH, $Mo_2TiC_2T_x$ and $CoOOH/Mo_2TiC_2T_x$ heterostructure were established for DFT calculations. The OER process in alkaline media involves the *, OH*, O* and OOH* intermediates, where * stands for the active sites. Moreover, the step with the largest change in Gibbs free energy ($\Delta G$) is considered to be the rate-determining step (RDS). As displayed in Fig. 4d, the RDS of CoOOH is the formation of OOH* intermediate from the O*, with the largest free energy barrier of 1.63 eV. For $Mo_2TiC_2T_x$, the OOH* intermediate reacts with $OH^-$ and further converts into $O_2$ is the RDS, with the largest free energy barrier of 2.76 eV. As for the $CoOOH/Mo_2TiC_2T_x$, the generation of O* from OH* is the RDS, and the free energy barrier is 1.41 eV. The reduction of RDS energy barrier reveals that the coupling of $Mo_2TiC_2T_x$ onto the CoOOH can optimize the intermediate adsorption and provide favourable OER kinetics, thereby enhancing the OER catalytic activity.

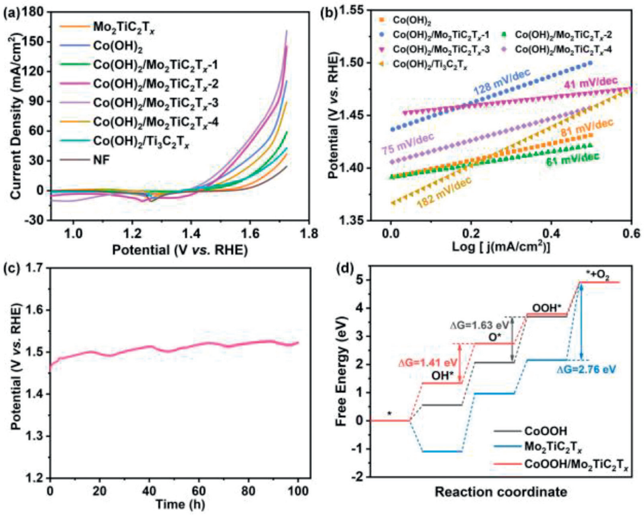

**Fig. 4.** OER performances of catalysts coated on NF: (a) Polarization curves. (b) The corresponding Tafel plots. (c) Chronopotentiometry of $Co(OH)_2/Mo_2TiC_2T_x$-3 at 10 mA/cm$^2$. (d) Free energy diagram for OER process on catalysts.

In summary, we have successfully prepared $Co(OH)_2/Mo_2TiC_2T_x$ hetero-nanosheets as efficient catalysts for OER *via* a simple MOF-derivative method at room temperature. The introduction of $Mo_2TiC_2T_x$ effectively optimizes the electronic structures of $Co(OH)_2$, leading to improved reactivity and conductivity. Moreover, the hetero-nanosheets offer rich active sites and ensure structural stability. With these merits, the optimal $Co(OH)_2/Mo_2TiC_2T_x$ hetero-nanosheets deliver excellent OER performance and good stability. Besides, the OER activity of $Co(OH)_2/Mo_2TiC_2T_x$ is superior to that of $Co(OH)_2/Ti_3C_2T_x$, indicating the advantage of double transition metal carbide as a substrate material. Therefore, this work not only provides an economical and convenient strategy for designing advanced electrocatalysts for OER but also expands the breadth of study in double transition metal MXenes.

## Declaration of competing interest

The authors declare that they have no known competing financial interests or personal relationships that could have appeared to influence the work reported in this paper.

## Acknowledgments

This work was supported by the National Natural Science Foundation of China (Nos. 22371165, 21971143, 22209098), the Natural Science Foundation of Hubei Province (No. 2022CFB326), the 111 Project (No. D20015), ITOYMR in the Higher Education Institutions of Hubei Province (No. T201904), the Key Project Foundation of Hubei Three Gorges Laboratory (No. Z2022078) and the Opening Foundation of Hubei Three Gorges Laboratory (No. SK213002). The authors also thank beamlines MCD-A and MCD-B (Soochow Beamline for Energy Materials) of the National Synchrotron Radiation Laboratory (Hefei, China) for providing soft X-ray absorption spectrometry testing.

## Supplementary materials

Supplementary material associated with this article can be found, in the online version, at doi:10.1016/j.cclet.2024.109774.

## References

[1] M. Lao, P. Li, Y. Jiang, et al., Nano Energy 98 (2022) 107231.
[2] P. Zhou, G. Hai, G. Zhao, et al., Appl. Catal. B: Environ. 325 (2023) 122364.
[3] K. Zhang, R. Zou, Small 17 (2021) 2100129.
[4] C. Xu, X. Yang, S. Li, et al., Inorg. Chem. Front. 10 (2023) 85–92.
[5] T.K. Das, T. Ping, M. Mohapatra, et al., Chem. Comm. 58 (2022) 3689–3692.
[6] Y.J. Son, S. Kim, V. Leung, et al., ACS Catal. 12 (2022) 10384–10399.
[7] M. Jiang, H. Zhai, L. Chen, et al., Adv. Funct. Mater. (2023) 2302621.
[8] Y. Zhou, J. Hu, L. Yang, Q. Gao, Chin. Chem. Lett. 33 (2022) 2845–2855.
[9] S. Liu, R.T. Gao, M. Sun, et al., Appl. Catal. B: Environ. 292 (2021) 120063.
[10] Y. Tong, J. Xu, H. Jiang, F. Gao, Q. Lu, Chem. Eng. J. 316 (2017) 225–231.
[11] H. Liu, D. Guo, W. Zhang, R. Cao, J. Mater. Res. 33 (2018) 568–580.
[12] L. Gao, Y. Li, G. Li, J. Huo, L. Jia, Chem. Eng. J. 451 (2023) 138743.
[13] G. Li, C. Liu, Z. Zhang, et al., J. Mater. Sci. Technol. 81 (2021) 131–138.
[14] C. Gong, L. Zhao, D. Li, et al., Chem. Eng. J. 466 (2023) 143124.
[15] X. Dong, Z. Xin, D. He, et al., Chin. Chem. Lett. 34 (2023) 107459.
[16] J. Zhang, Y. Wang, H. Wang, D. Zhong, T. Lu, Chin. Chem. Lett. 33 (2022) 2065–2068.
[17] L. Chen, Y. Guo, H. Wang, et al., J. Mater. Chem. A 6 (2018) 4636–4641.
[18] X. Xu, Z. Zhong, X. Yan, L. Kang, J. Yao, J. Mater. Chem. A 6 (2018) 5999–6006.
[19] J.M. Huo, Y. Wang, J. Meng, et al., J. Mater. Chem. A 10 (2022) 1815.
[20] M. Huang, W. Liu, L. Wang, et al., Nano Res. 13 (2020) 810–817.
[21] C. Jiang, S. Li, B. Li, et al., Dalton Trans. 50 (2021) 3060–3066.
[22] B. Shen, Y. Feng, Y. Wang, et al., Carbon 212 (2023) 118141.
[23] X. Zhao, X. Ding, Y. Xia, et al., ACS Appl. Nano Mater. 1 (2018) 1476–1483.
[24] Z. Liu, Z. Guo, H. He, et al., Int. J. Hydrog. Energy 47 (2022) 40986.
[25] R. Cheng, Y. Min, H. Li, C. Fu, Nano Energy 115 (2023) 108718.
[26] Y. Zhang, Y. Lin, T. Duan, L. Song, Mater. Today 48 (2021) 115–134.
[27] L. Li, D. Yu, P. Li, et al., Energy Environ. Sci. 14 (2021) 6419–6427.
[28] S. Zhang, X. Xu, X. Liu, et al., Mater. Horiz. 9 (2022) 1708–1716.
[29] D. Guo, F. Ming, D.B. Shinde, et al., Adv. Funct. Mater. 31 (2021) 2101194.
[30] X. Zhang, J. Miao, P. Zhang, et al., Chin. Chem. Lett. 31 (2020) 2305–2308.
[31] X. Liu, F. Xu, Z. Li, et al., Coord. Chem. Rev. 464 (2022) 214544.
[32] X. Yang, C. Xu, S. Li, et al., J. Colloid Interface Sci. 617 (2022) 633–640.
[33] L. Li, Comput. Mater. Sci. 124 (2016) 8–14.
[34] J. Peng, X. Chen, W.J. Ong, X. Zhao, N. Li, Chem 5 (2019) 18–50.
[35] J. Zhang, Y. Zhao, X. Guo, et al., Nat. Catal. 1 (2018) 985–992.
[36] L.H. Zheng, C.K. Tang, Q.F. Lü, J. Wu, Int. J. Hydrog. Energy 47 (2022) 11739–11749.
[37] R. Khaledialidusti, A.K. Mishra, A. Barnoush, J. Mater. Chem. C 8 (2020) 4771–4779.
[38] W. Ren, Z. Chang, J. Zhang, L. Wang, C. Xu, ACS Appl. Energy Mater. 5 (2022) 15828–15833.
[39] B. Anasori, C. Shi, E. Moon, et al., Nanoscale Horiz. 1 (2016) 227.
[40] J. Wang, P. He, Y. Shen, et al., Nano Res. 14 (2021) 3474–3481.
[41] Y. Wang, A. Li, C. Cheng, Small 17 (2021) 2101720.
[42] X. Yang, Y. Tian, S. Li, et al., J. Mater. Chem. A 10 (2022) 12225–12234.
[43] M. Pan, X. Zhang, C. Pan, J. Wang, B. Pan, ACS Appl. Mater. Interfaces 15 (2023) 19695–19704.
[44] J. Li, D. Chu, D.R. Baker, et al., Chem. Mater. 31 (2019) 7590–7600.
[45] Y. Tong, Y. Guo, P. Chen, et al., Chem 3 (2017) 812–821.
[46] Z.J. Zhang, J.P. Guo, S.H. Sun, et al., Rare Metals 42 (2023) 3607–3613.
[47] M. Tahir, L. Pan, R. Zhang, et al., ACS Energy Lett. 2 (2017) 2177–2182.